Chemical Geology 678 (2025) 122676

Contents lists available at ScienceDirect

Chemical Geology

journal homepage: www.elsevier.com/locate/chemgeo

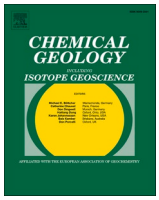

Apatite and magnetite as probes into dissimilatory iron reduction in banded iron formations

Tianyang Hu [a,b,c], Leslie J. Robbins [c], Kurt O. Konhauser [d], Lei Liu [a,*], Brendan A. Bishop [c], Guoxiang Chi [c], Lijuan Xu [e]

[a] Key Laboratory of Metallogenic Prediction of Nonferrous Metals and Geological Environment Monitoring, Ministry of Education, School of Geosciences and Info-Physics, Central South University, Changsha 410083, China
[b] Henan Academy of Geology, Zhengzhou 450016, China
[c] Department of Earth Sciences, University of Regina, Regina, SK, Canada
[d] Department of Earth & Atmospheric Sciences, University of Alberta, Edmonton, Alberta, Canada
[e] School of Earth Resources, China University of Geosciences, Beijing 100083, China

ARTICLE INFO

Editor: Marco Fiorentini

Keywords:
Apatite
Magnetite
Dissimilatory iron reduction
Microbial activity

ABSTRACT

Banded iron formations (BIFs) are ancient sedimentary deposits that provide critical insights into the evolution of Earth's early atmosphere, hydrosphere, and biosphere. This study focuses on the Ouyang BIF in the North China Craton (NCC), highlighting the substantial impact of dissimilatory Fe(III) reduction (DIR) on both the remobilization of iron from the primary iron precipitates and subsequent authigenic mineralization during diagenesis. This biological process is manifested in the light iron isotopes in magnetite (δ^{56}Fe values down to -2.1 ± 0.02 ‰) and distinct geochemical signatures in associated apatite. Specifically, the elevated Mn/U ratios (ranging from 467 to 1210) in apatite indicates redox cycling, while elevated concentrations of Sr (ranging from 15,453 to 20,466 ppm), and OH (33 % to 58 % in molar) in apatite are characteristic of biomineralization processes during BIF formation. The relationship observed between Sm/Nd ratios (and Nd isotopes) in apatite and δ^{56}Fe values in magnetite further suggests that iron was sourced to the Wuyang BIFs from both hydrothermal fluids and a benthic iron flux. Notably, the benthic Fe flux likely resulted from the DIR of ferric oxyhydroxide minerals in nearshore sediments, highlighting the essential role of continental iron and DIR in transporting Fe from the continents to BIF depositional centers. This study underscores the critical influence of microbial activity in iron cycling within ancient oceans. It further showcases how DIR was recorded by apatite and magnetite, offering insights into past DIR bacteria during BIF deposition.

1. Introduction

Banded iron formations (BIFs) are iron- and silica-rich chemical sedimentary rocks that precipitated from the water column during much of the Precambrian eon (see Konhauser et al., 2023 for review). It is widely accepted that bacteria played a crucial role in their genesis. This includes the initial oxidation of dissolved Fe^{2+} into ferric oxyhydroxides (e.g., ferrihydrite) within the water column to and subsequent transformations within the sediment pile during diagenesis and metamorphism. These processes yield minerals like magnetite, siderite, and various ferrous-silicates. During diagenesis, dissimilatory iron reduction (DIR) may occur, where the ferric iron in ferrihydrite is reduced while cell biomass, co-deposited with ferrihydrite in aggregate form, is oxidized (Köhler et al., 2013; Posth et al., 2014; Halama et al., 2016; Li, 2021, 2024). Despite the significant role that DIR may play in BIF diagenesis, microfossil evidence within BIFs is notably absent. One explanation is that the biomass was degraded during DIR (Konhauser et al., 2005). Alternatively, it has been suggested that Fe(II) oxidizing bacteria and ferrihydrite may have segregated within the water column, with bacteria shedding the particles, as proposed by Konhauser et al. (2005) and Thompson et al. (2019), while silica components induce a repulsion between the cell surfaces of photoferrotrophs and iron (oxyhydr)oxides, leading to the formation of BIFs with limited organic content.

Given the lack of preserved microfossils and minimal organic carbon in BIFs, the primary evidence supporting the hypothesis of microbial

* Corresponding author.
E-mail address: liu01@ustc.edu.cn (L. Liu).

https://doi.org/10.1016/j.chemgeo.2025.122676
Received 21 May 2024; Received in revised form 4 February 2025; Accepted 4 February 2025
Available online 6 February 2025

involvement, specifically DIR during BIF formation includes: (1) the association of apatite with graphite and the depleted organic carbon isotopic composition of BIFs which suggests a microbial influence on mineral precipitation (Li et al., 2011, 2013a; Dodd et al., 2019); (2) the antiquity of hyperthermophilic Bacteria and Archaea branches on the universal phylogenetic tree and their ability to conduct DIR which supports the plausibility of microbial activity in paleo-environments (Vargas et al., 1998; Li et al., 2011); and (3) experimental results that demonstrate that the DIR process leads to the depletion of heavy Fe isotopes in Fe^{2+}, and magnetite in BIFs, as a Fe^{2+}-bearing diagenetic minerals, record this isotopic signature (Johnson et al., 2005, 2008; Amor et al., 2018). However, it has been questioned whether these observations can be solely attributed to the presence and activity of DIR bacteria during BIF formation. For example, based on SEM petrological observations, Lepland et al. (2005) noted the absence of graphite inclusions within apatite crystals, challenging the presumed link between apatite and signs of early microbial life. However, their study focused on Eoarchean rocks, which may limit the applicability of their findings to the full BIF record. Furthermore, Rasmussen et al. (2017, 2021a, 2021b), using optical microscopy, scanning electron microscopy, and transmission electron microscopy on various BIFs, identified greenalite nanoparticles, suggesting that the primary sedimentary minerals of BIFs might be ferrous silicates rather than Fe(III)-bearing phases. These findings raise the possibility that the formation of magnetite and siderite in BIFs could occur without DIR, challenging the paradigm that biological processes were a necessity for BIF deposition.

A potential resolution to this debate may be found through further examination of BIF samples containing a mineral assemblage including apatite and magnetite, coupled with light iron isotope compositions. Such a multifaceted approach, integrating mineralogical and geochemical analyses, could elucidate whether the iron isotope signatures observed in these BIF samples originated from later post-depositional transformations or were inherited from the original marine sediments. This investigation could provide insight into whether microbial activity played a role in the mineralization of BIFs. The Wuyang BIF, located on the southern margin of the North China Craton (NCC), exhibits these aforementioned characteristics (Lan et al., 2019; Duan et al., 2021). Consequently, this study examines the trace elements and isotopic composition of apatite and magnetite from the Wuyang BIF. By combining these findings with previous research on DIR, this study aims to ascertain whether microbial activity contributed to the formation of BIFs or if they resulted from abiogenic mineralization processes.

2. Geological Background

2.1. BIFs in NCC and the Lushan-Huoqiu BIFs Belt

The NCC, China's largest and oldest craton, stands as the principal repository for iron deposits in the nation. Significant accumulations of iron are predominantly concentrated in the regions of Luoshan, Wuyang, Huoqiu, and Xincai, all located along the southern periphery of the NCC (Zhai and Windley, 1990; Lan et al., 2017; Liu et al., 2018). The Neoarchean era, specifically between 2550 and 2500 Ma, represents the peak period of BIF deposition in China, although a few sporadic deposits emerged during the Paleoproterozoic (e.g., Wuyang and Yuanjiacun), Mesoproterozoic (e.g., Jingtieshan-type), and Neoproterozoic eras (e.g., Xinyu and Shilu) (Wan et al., 2012; Zhang et al., 2012; Li et al., 2015a). Algoma-type BIFs from the Archean era are mainly located in the northern region of the NCC, whereas Paleoproterozoic Superior-type BIFs are found in the central to southern regions of the craton (Zhang et al., 2014). The Lushan-Huoqiu BIF Belt (LHBB), located on the southeast margin of NCC, has been the focal point of previous studies. Lan et al. (2017) investigated the lithology of the Upper Taihua Group, encompassing the Wuyang, Lushan, Xiong'er Mountain, and Xiaoqinling regions along the craton's southern edge (Fig. 1). Their work determined the sedimentary age and revealed stratigraphic continuity across these regions. Subsequently, several studies identified consistent characteristics within the BIFs from the Wugang, Huoqiu, and Xincai regions, prompting speculation regarding the existence of an expansive BIF ore belt along the southern border of the NCC (Such as Liu et al., 2018; Hu et al., 2024). They also suggested the prevalence of Superior-type BIFs along the craton's southern margin.

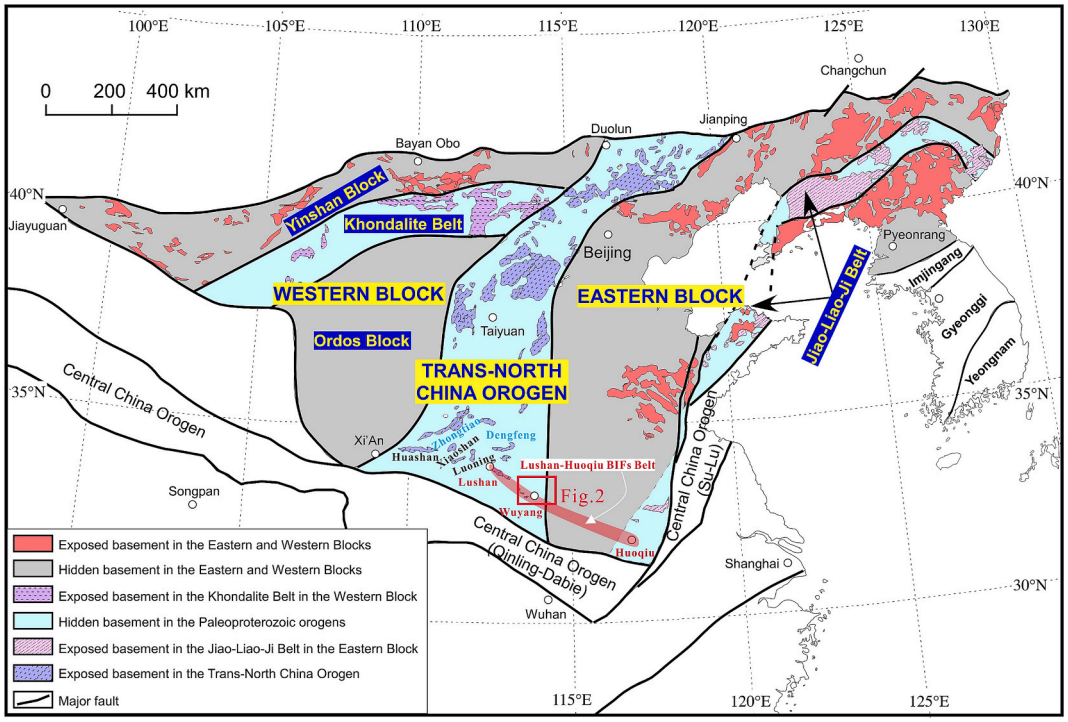

Fig. 1. The North China Craton (NCC) map showing tectonic subdivision of exposed Archean to Paleoproterozoic basement (revised after Zhao et al., 2005).

2.2. Stratigraphy of the Wuyang BIFs

Central to the LHBB lies the Wuyang BIFs, primarily hosted within the Taihua Complex (Fig. 2). This complex is oriented northwest-southeast, sporadically emerging at the surface over hundreds of kilometers (Diwu et al., 2014). In the Wuyang region, the Taihua Complex can be subdivided into three main formations: Zhao'anzhuang (ZAZ), Tieshanmiao (TSM), and Yangshuwan (YSW) (Fig. 2). The basal section of the ZAZ Formation comprises marine volcanic rocks consisting of iron-rich serpentinite, diopside amphibolite, and komatiites. Moving upwards, the ZAZ Formation transitions into the khondalite series (a regional metamorphic rock assemblage with garnet, sillimanite, and graphite enrichment), characterized by a garnet-rich schist. The dominant lithologies include amphibolite, amphibole schist, almandine-amphibole-plagioclase gneiss, biotite plagiogneiss, and phlogopite plagiogneiss. The ore-bearing segments A and B are contained within this formation, with a depositional age older than 2470 ± 40 Ma, as suggested by the youngest seven detrital zircons from the lower part of the ZAZ Formation yielding a weighted mean $^{207}Pb/^{206}Pb$ age (Lan et al., 2017). The overlying TSM Formation, approximately 1000–1500 m in thickness, is characterized by migmatite and gneiss, which is prevalent in the Jingshansi, Xiaohanzhuang, Shangmiao, and Shimen regions (Yao et al., 2015; Liu et al., 2018). Stratigraphic markers associated with BIFs in the TSM Formation include banded quartz-pyroxene-magnetite interspersed with marble. Its primary constituents range from migmatite, biotite-plagioclase gneiss, amphibole-plagioclase gneiss, and quartz-pyroxene magnetite to magnetite-quartz-pyroxene assemblages, interlayered with plagioclase-amphibole-gneiss and marble (Liu et al., 2018; Lan et al., 2019). Lastly, the YSM Formation is composed of banded migmatite, oligoclase-amphibole-gneiss, and graphite-oligoclase-amphibole-gneiss. Its lower strata interface with the underlying TSM Formation through either an unconformable or faulted contact and with the overlying Xiong'er Group through a non-conformable contact. Its middle strata consist of sillimanite oligoclase-gneiss and graphite-oligoclase-amphibole-gneiss, while its basal layer features banded migmatite with a depth exceeding 960 m. The upper part of the YSW Formation is composed of felsic granulite (Lan et al., 2019).

2.3. Geological Features and Geochronology of the Wuyang BIFs

The Tieshanmiao BIF (TSMB), situated within in the TSM Formation, are distributed across two distinct ore-bearing segments, labelled C and D (Fig. 2). The TSM Formation can be further divided into eight lithological segments, from the base upwards: (1) migmatite; (2) the C ore segment; (3) amphibole gneiss; (4) banded migmatite; (5) almandine-amphibole-plagioclase gneiss; (6) D ore segment; (7) marble interlayered with amphibolite; and (8) a secondary banded migmatite unit (Li et al., 2013b). The basal migmatite layer is approximately 400 m thick and can be observed predominantly in the Jinghansi areas.

The C ore segment is composed of variegated marble hosting various types of quartz-pyroxene-magnetite layers. The ore body has a stratiform or lenticular shape, ranging from 20 to 40 m in thickness, with a maximum thickness of 70 m. The lowermost ore-bearing zone within the amphibolite gneiss features an angular unconformity with the overlying mixed rock, with a thickness of 10 to 300 m.

The D ore segment ranges in thickness from 11 to 268 m, averaging 114 m, and primarily consists of banded quartz-pyroxene-magnetite and massive magnetite interspersed with dolomitic marble, pyroxenite, iron-bearing quartzite, and oligoclase hornblende biotite schist. The marble interlayered with the amphibolite unit is mainly composed of serpentine marble or coarse-grained marble, interlayered with amphibolite, pyroxene rock, or biotite schist, and has a thickness ranging from 2 m to 47 m. The second banded migmatite unit consists of mixed granite and amphibolite, with a thickness of over 500 m.

Zircons extracted from the basal layers of the ZAZ Formation exhibit distinct magmatic characteristics. Lan et al. (2017) determined a weighted mean age of 2470 ± 40 Ma for the youngest detrital zircon within this formation. Conversely, Duan et al. (2021) obtained an upper intercept age of 2406 ± 24 Ma from the overlying pyroxene biotite gneiss, establishing a timeline for the BIF's deposition. Consequently, deposition of the TSM Formation and TSMB is constrained to between 2470 and 2406 Ma, placing it within the early Paleoproterozoic era concurrent with the onset of the Great Oxidation Event (GOE).

The whole-rock TSMB samples exhibit seawater-like REE patterns, characterized by LREE depletion, positive anomalies of La, Gd, and Y, and high Y/Ho ratios, indicating that seawater played a role in the formation of TSMB (Lan et al., 2013, 2019; Li et al., 2013a, 2013b; Yao

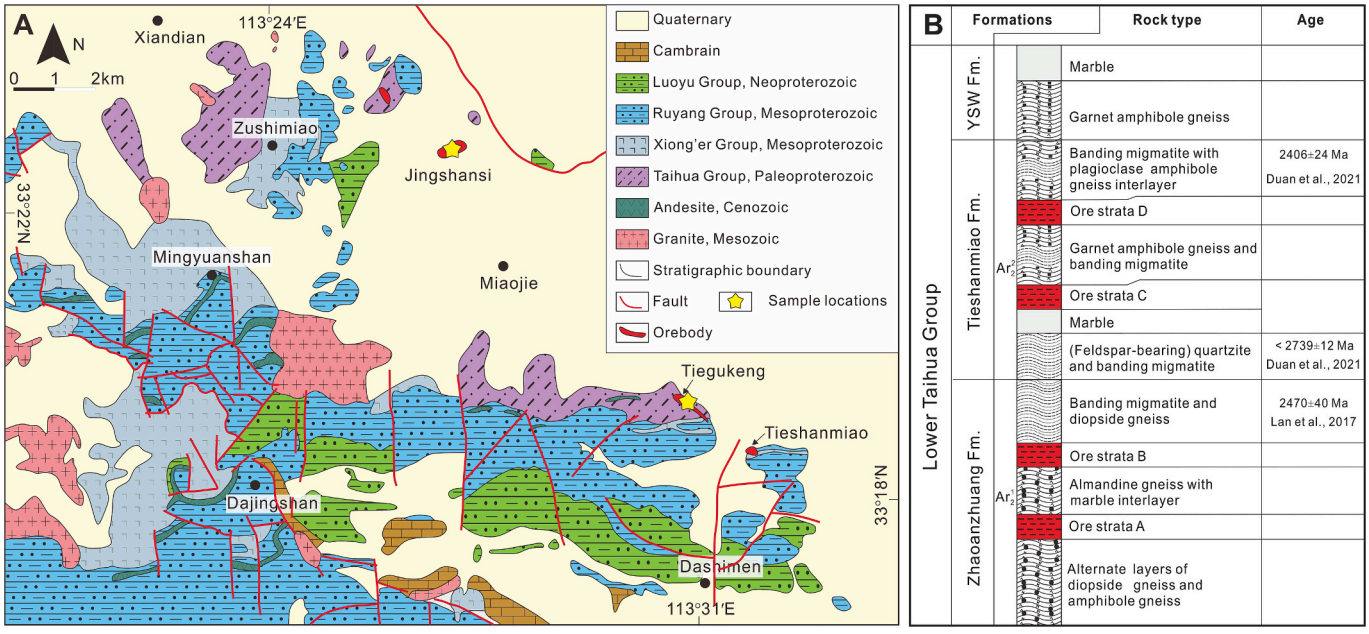

Fig. 2. (A) Geological map of the Wuyang area (modified after Han, 2010; Li et al., 2013b); (B) Generalized stratigraphic column for the Taihua complex Li et al. (2014). Iron ore strata A and B belong to Zhaoanzhuang Formation, whereas C and D belong to Tieshanmiao Formation.

et al., 2015; Liu et al., 2018; Duan et al., 2021). The protoliths of the surrounding rocks of the TSMB include iron-bearing dolomitic mudstone for the amphibolite, dolomitic marble for the marble, and dolomitic mudstone for the calc-magnesian silicate rocks (Lan et al., 2013). Additionally, the TSMB samples show relatively high average Eu anomalies of 1.71, with negative δ^{56}Fe values ranging from −1.248 to −0.012 ‰ (average = −0.626 ‰; Lan et al., 2019; Duan et al., 2021). The Fe isotopic composition of TSMB is similar to that of the Fe-bearing mineral phases in Superior-type Kuruman and Brockman BIFs (−2.2 to 0 ‰; Steinhoefel et al., 2010), suggesting TSMB belongs to Superior-type BIFs (Duan et al., 2021).

3. Sampling Rationale and Petrological Observation

Samples from the TSMB were collected from the Jingshansi and Tiegukeng mining sites, located at coordinates 33°23′33″ N, 113°25′54″ E and 33°20′28″ N, 113°31′20″ E, respectively, as shown in Fig. 2. At the Tiegukeng deposit, the surrounding rock mainly composed of marble, with a conspicuous massive layered and banded mixed rock unit visible at its summit (Fig. 3a). In contrast, at the Jingshansi deposit, a leptite rock layer formed both the roof and floor, while the iron ore layer extended northwestward, progressively thickening in a lens-shaped morphology (Fig. 3b). The ore body is layered, with two types of ore: banded pyroxene-magnetite quartzite (BPMQ) and disseminated quartz magnetite pyroxenite (DQMP) (Fig. 3c-e). In both ore types, quartz, magnetite, and clinopyroxene grains displayed typical triple junction contacts, indicative of mineral equilibrium features (Lan et al., 2017).

The BPMQ rocks are typically black-gray and dark green-gray in colour, with a banded structure with widths ranging from 0.5 to 2 cm. These rocks are primarily composed of pyroxene, magnetite, quartz, and accessory minerals such as apatite and zircon. Within the BPMQ, white quartz bands are prevalent. Based on the occurrence of garnet and the amount of hornblende, the BPMQ rocks are further categorized into two types: Type-I BPMQ (BPMQ-I) and Type-II BPMQ (BPMQ-II). Type-I BPMQ is characterized by samples 20WG-4 and 20WG-10, where the total pyroxene content is approximately 35 %, and is comprised of clinopyroxene and hypersthene (Fig. 3f). Clinopyroxene grains vary in size from 0.1 to 0.4 mm, appearing yellow-green or transparent, and are often associated with hornblende and magnetite, while hypersthene appears pale pink (Fig. 3 f, g). Similarly, the magnetite content is approximately 35 %, with grain sizes of approximately 0.2 mm, occurring as interstitial minerals between pyroxene or quartz. Quartz occurs as subhedral crystals (0.2–0.5 mm), with white bands measuring 1–2 mm in width. Iron-rich bands consist of calcium-rich monoclinic pyroxene and magnetite, with certain silica-rich bands containing magnetite particles within the quartz matrix (Fig. 3e). In contrast, Type-II BPMQ, exemplified by sample 20WG-9, exhibits a hornblende content of approximately 25 %, with grain sizes ranging from 0.5 to 1.5 mm. The hornblende is associated with garnet, apatite, and magnetite (Fig. 3h). Quartz occurs as subhedral crystals (0.2–0.5 mm), with white bands reaching widths of about 2–3 mm, predominantly composed of quartz. Magnetite grains are either dispersed in the quartz matrix within certain silica-rich bands or associated with hornblende (Fig. 3h).

The DQMP type rock, which includes samples 20WG2–13 and

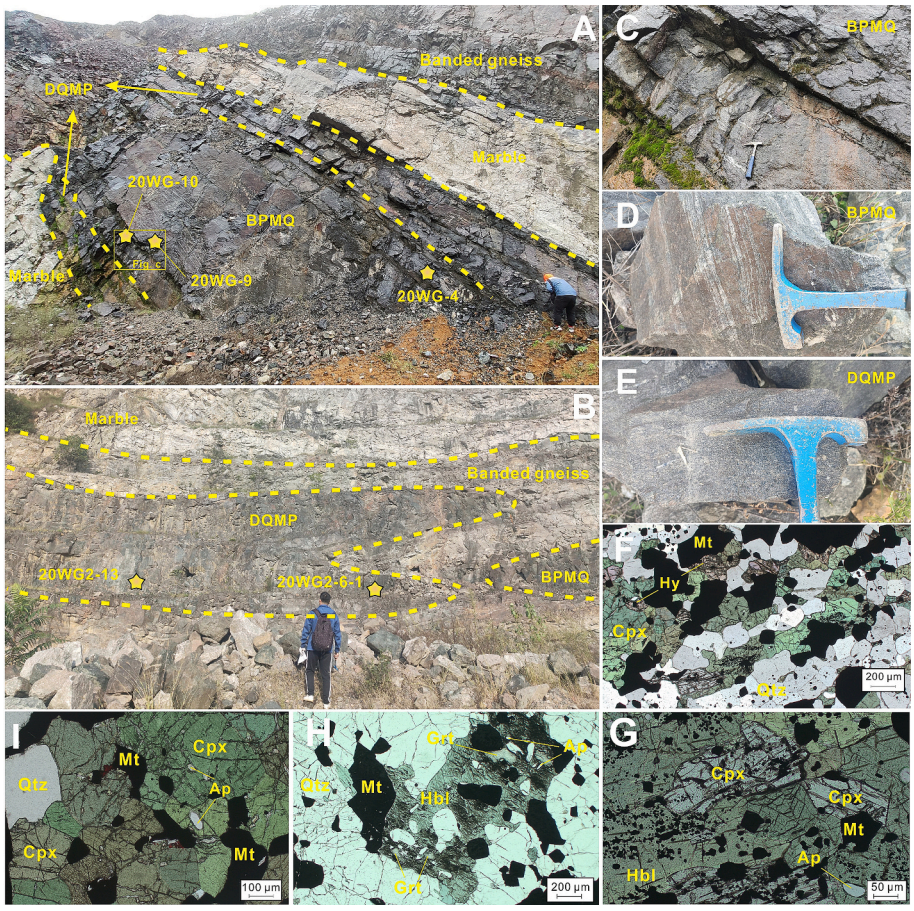

Fig. 3. Field photos and photomicrographs of Wuyang rocks. (A) Field photo of Tiegukeng mining area, with massive layered and banded rocks; (B) Field photo of Jingshnansi mining area; (C, D) Banded pyroxene-magnetite quartzite (BPMQ) with band width of 1–2 cm; (E) Photomicrographs of Disseminated quartz magnetite pyroxenite (DQMP); (F—H) Photomicrographs of BPMQ; (I) Photomicrographs of DQMP. Abbreviations: Qtz - Quartz, Grt - Garnet; Mt. - Magnetite; Cpx - Clinopyroxene; Ap - Apatite; Bt - Biotite.

20WG2–6-1, appears as yellow-green and gray-green, displaying a disseminated texture and occasionally forming iron-rich mineral veins within the ore body (Fig. 3i). This ore mainly comprises pyroxene (approximately 55 %) and magnetite (approximately 35 %), with garnet, quartz, and apatite as accessory minerals (Fig. 3i). The pyroxene is predominantly clinopyroxene, exhibiting euhedral morphology with a grain size of approximately 0.4 mm. Magnetite appears as infiltrations or partially euhedral crystals, with grain sizes ranging from 0.1 to 0.2 mm. It is interstitial to the clinopyroxene, suggesting a co-genetic or slightly later formation compared to the pyroxene (Fig. 3i).

4. Analytical methods

Apatite and magnetite were separated from crushed whole rock samples using flotation and magnetic separation methods, respectively. These mineral separation procedures were conducted at the Nanjing Hongchuang Geological Company. Following separation, apatite grains were embedded into epoxy resin mounts for subsequent experimental analysis.

4.1. In-situ Apatite Analysis

Major elemental analysis of apatite from the TSMB was performed via Electron Micro-Probe Analysis (EMPA) using a JEOL JXA-iSP100 electron microprobe at the Hong-Chuang Geological Exploration Technology Service Co. in Nanjing, Jiangsu province. Operating parameters included an accelerating voltage of 15 kV, beam current of 20 nA, and a 20 μm beam diameter. Selected crystals for the assessment included LDE1 (F), TAP (Al, Si, Na, Mg, Sr), PETJ (P, S, K, Ca), PETH (Cl), and LIFH (Ti, Fe, Mn). Element counting durations were set at 20 s for P, Ca, Ti, Si, Al, Fe, Mn, Mg, and K, and 10 s for Na, F, and Cl at peak position. The background signal was analyzed for half the peak duration. With the exception of Sr (analyzed via the Lα line), the Kα line was used for all elements. Reference standards included fluorapatite (F, P, Ca), almandine (Al), diopside (Si), albite (Na), olivine (Mg), celestite (Sr), orthoclase (K), rutile (Ti), hematite (Fe), rhodonite (Mn), and tugtupite (Cl). The ZAF correction standards were applied to all results.

Determination of in situ trace elements in the TSMB apatite was conducted at the Key Laboratory of Metallogenic Prediction and Monitoring of Ministry of Education at Central South University in Changsha, Hunan. Analysis was performed using a Teledyne Photon Machines laser ablation system and an Analytik Jena Plasma Quant MS Elite mass spectrometer (LA-ICP-MS) to measure the trace element composition of individual apatite samples. The laser spot size was 35 μm, with the repetition rate of 5 Hz, a beam energy of 1.5 to 2.5 J/cm^2, and the analysis time for a single spot was 80 s (including 30 s of background measurement, 30 s of signal analysis, and 20 s of washout time). GSE-2G and GSE-1G were used as system monitoring samples and the glass standards NIST 610 and 612 were used as the external calibration standards. Calcium content obtained from EMPA was used as the internal standard. The accuracy for most analyses was better than 5 %, with the limit of detection (LOD) well below the ppm range. Data reductions used GLITTER 4.4.4 (developed by GEMOC), and were carried out according to the standard method (Griffin, 2008).

The in situ apatite Sm—Nd isotopic compositions were obtained using a Neptune Plus MC-ICP-MS (Thermo Fisher Scientific, Bremen, Germany) paired with a Geolas Pro excimer ArF laser ablation system (Coherent, Göttingen, Germany) at Xi'an Center of Geological Survey's Isotopic lab in Shanxi, China. Analysis was done in single point mode, which employed a 60 μm laser beam spot size, 8 Hz laser ablation rate, and a consistent laser energy density of ~10 J/cm^2. Each point accumulated data from 300 cycles: the initial 60 cycles (18.78 s) recorded background signals for interference deduction, the subsequent 20 cycles (6.26 s) captured signal transition, and the last 220 cycles (68.86 s) gathered sample erosion signals, with the ion signals being received by eight Faraday cup detectors. The experimental approach commenced with the determination of Nd isotopic ratios using interference-corrected $^{146}Nd/^{144}Nd$ measured values alongside natural abundance ratios. The fractionation factors for Nd isotopes were then calculated, followed by the determination of true values for $^{143}Nd/^{144}Nd$, $^{145}Nd/^{144}Nd$, and $^{147}Sm/^{144}Nd$, using the exponential normalization method. The natural abundance ratios employed in the calculations were as follows: $^{147}Sm/^{149}Sm = 1.08680$, $^{144}Sm/^{149}Sm = 0.22332$, and $^{146}Nd/^{144}Nd = 0.7219$. All data processing was conducted using the laboratory's internal software, Nada 1.0. To monitor and validate the reliability of the in-situ micro-area Nd isotopic testing and calibration methodologies, the $^{143}Nd/^{144}Nd$ values of three natural apatite standards were utilized (Yang et al., 2014): Durango (0.512490 ± 0.000046), Otter Lake (0.511942 ± 0.00004), and Mud Tank (0.512361 ± 0.000111). These standards served as benchmarks to ensure the accuracy and reliability of the unknown sample analysis throughout the experimental process.

4.2. Magnetite Fe Isotopic Analysis

Iron isotopic analysis was performed at the China University of Geosciences (Beijing), Isotope Geochemistry Lab and the Hefei University of Technology, School of Resources and Environmental Engineering, on a Thermo Fisher Neptune Plus MC-ICPMS. Both labs maintained identical analytical procedures and equipment settings to ensure consistency. Prior to isotopic analysis, the, Fe element was isolated following standard cation exchange column procedures (details in Li et al., 2022). Samples were processed using a PFA micro-nebulizer and a quartz glass spray chamber. Iron isotopes were measured at the lower mass shoulders in high-resolution modes with ^{53}Cr, ($^{54}Cr + {}^{54}Fe$), ^{56}Fe, ^{57}Fe, ($^{58}Fe + {}^{58}Ni$), and ^{60}Ni statically collected by Faraday cups, L3, L1, C, H1, H2, and H4, respectively. Isotopic values were averaged from four repeat tests and uncertainties defined within specific parameters. Analysis involved a specific sequence of steps and cycles, using GSB Fe as a reference (details in Li et al., 2022). The Fe isotopic composition is expressed in delta (δ) units relative to the IRMM-014 standards: $\delta^{56}Fe\ (‰) = [(^{56}Fe/^{54}Fe)_{sample} / (^{56}Fe/^{54}Fe)_{IRMM\text{-}014} - 1] \times 1000$. The $\delta^{56}Fe$ values of standard samples are 0.106 ± 0.023 ‰ (AGV-2) and 0.154 ± 0.017 ‰ (GSP-2), which agree with accepted values.

5. Results

5.1. Morphology and Chemical Composition of Apatite

The separated apatite grains from TSMB exhibit homogeneity under backscattered electron (BSE) imaging (Fig. S1). In the DQMP samples, grains appear clean without noticeable zoning, although there was a considerable variation in particle size among different samples. For instance, sample 20WG2–6 consists of small grains, ranging from 50 to 150 μm, and elongated particles with a 2:1 to 3:1 aspect ratio measuring 150 to 250 μm in length. In contrast, the grains in sample 20WG2–13 are significantly larger, ranging from 100 to 300 μm. The BPMQ-I samples generally feature larger grain sizes. Sample 20WG-4 consists of square particles of approximately 150 μm in size and elongated particles ranging from 200 to 250 μm, also with a 2:1 aspect ratio. These samples exhibit red coloration within the grains, which may be indicative of the presence of hematite. Sample 20WG-10 contains larger elongated grains measuring 200 to 300 μm, with clean, uncracked surfaces and no evident zoning. The BPMQ-II samples are free of cracks and discernible zoning, with a distinct size gradation including particles around 50 μm, as well as elongated grains measuring 200 to 250 μm with a 2:1 aspect ratio.

Results for the major and trace element analysis for the apatite grains are presented in Table S1. The molar proportions of F, Cl, and OH (denoted as XF, XCl and XOH, respectively) in three samples are shown in Fig. 4. Among all three types of apatite, the BPMQ-II samples contained the highest XOH and Sr content (46 % to 58 % in molar and 15,453–27,175 ppm, respectively), while the DQMP samples showed the highest XF content and lowest Sr content (74 % to 90 % in molar and

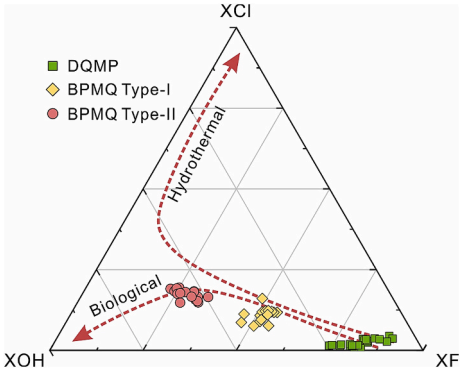

Fig. 4. Volatile components of four types of apatite from the TSMB, in comparison with those of three types of apatite. XCl, XOH, and XF are molar proportions of Cl, OH, and F in *Z*-site of apatite, respectively.

71–2016 ppm, respectively). All three types of apatite were enriched in light REEs (LREEs) (Fig. 5a-e), while the BPMQ-I samples show the most depleted heavy REEs (HREEs) (Fig. 5a, b). For sample 20WG2–6, although it appears less uniform compared to other samples in Fig. 5 due to the logarithmic scale, it exhibits a similar uniform Y/Ho (40–43) and Eu anomalies (1.4–1.6) to the other samples. Furthermore, all samples display positive Eu and Y anomalies characteristic of marine sediments (Bau and Dulski, 1996). BPMQ-II apatite also contain relatively high Mn content (637–910 ppm) and lower Th and U contents (2.83–7.75 ppm and 0.66–1.42 ppm, respectively), resulting in the highest Mn/U values among the three types of apatite (467–1210). In contrast, Mn/U values for BPMQ-I and DQMP apatite grains ranged from 4 to 132 and 5–47, respectively. The $^{143}Nd/^{144}Nd$ ratios of BPMQ-II apatite grains were relatively uniform (0.510238–0.510488) with primarily negative ε_{Nd} (t = 2.4 Ga) values ranging from −6.3 to −1.0 (Table 1). Compared with BPMQ-II apatite, BPMQ-I and DQMP apatite contained elevated ε_{Nd} (t) values (−4.1 to +0.4 and − 2.9 to +1.4, respectively).

5.2. Magnetite Fe isotopes

Iron isotopic signatures within the TSMB are expressed relative to the IRMM-14 standard, adopting the standard δ-notation as delineated in Table 1. BPMQ-II magnetite is distinguished by its markedly low $\delta^{56}Fe$ values of −2.1 ± 0.02 ‰, indicating a substantial depletion of the heavy iron isotope. Conversely, DQMP and BPMQ-I magnetite exhibit less pronounced, yet still notable, depletion in heavy iron isotopes, with $\delta^{56}Fe$ values ranging from −0.62 to −0.84 ‰ and − 0.96 to −1.36 ‰, respectively.

6. Discussion

6.1. Preservation of the chemical signals following metamorphism

The mobility of elements during fluid-rock interactions related to metamorphism must be considered before their use in petrogenetic interpretation. Fluid-rock interactions typically occur at temperatures between 500 °C and 600 °C (Bau, 1991), and in the case of TSMB, which underwent metamorphism at 760 °C, such interactions are expected (Lan et al., 2019). However, several factors suggest that fluid-rock interactions did not significantly alter the TSMB: (1) the absence of fluid-derived minerals such as calcite and fluorite in TSMB (Möller, 1983; Lan et al., 2019); (2) the notably lower K/Rb ratios in TSMB (K/Rb ⟨100) compared to granulite (K/Rb > 500) suggest that the TSMB may have not suffered significant REE loss since Rb is more fluid-mobile than REE + Y (Rudnick et al., 1985; Lan et al., 2019); and (3) Eu, which is more sensitive to remobilization under reducing conditions or high temperatures than other REE + Y (MacRae et al., 1992; Bilal, 1991), is consistently enriched relative to neighboring elements in the TSMB rocks, further suggesting limited fluid-rock interaction during metamorphism.

Trendall and Morris (1983) suggested that when the primary minerals in ore are quartz and magnetite, even under high-grade metamorphism, no metamorphic reactions would occur between the minerals. Instead, recrystallization is likely to take place, causing the mineral grains to become equigranular and coarse-grained. Additionally, it has been reported that when BIF undergoes metamorphism, especially during granulite facies metamorphism, the primary structural features may be altered, and primary layering may even be obliterated, but the REE + Y composition is likely retained (Bolhar et al., 2004; Friend et al., 2008; Roy and Venkatesh, 2009; Angerer et al., 2012). Moreover, initial differences in REE + Y contents and distributions across individual BIF bands are expected to diminish and become averaged during diagenesis and metamorphism (Haugaard et al., 2013; Bonnand et al., 2020). Modern seawater, when normalized to Archean shales, is characterized by positive La and Y anomalies, along with a negative Ce anomalies, while high-temperature hydrothermal fluxes tend to exhibit strong positive Eu anomalies (Bolhar et al., 2004; Planavsky et al., 2010). However, due to the less oxidizing nature of Archean-Paleoproterozoic seawater compared to the modern ocean, negative Ce anomalies are generally absent in marine, Archean chemical sediments (Konhauser et al., 2017). Consequently, as marine chemical sediments, Archean-Paleoproterozoic BIFs generally display positive La, Y and Eu anomalies (e.g., Bau and Dulski, 1996; Pecoits et al., 2009; Martins et al., 2022). The TSMB shows minimal effects from diagenesis, metamorphism, or alteration, especially with respect to trace elements and REE + Y patterns (e.g., Liu et al., 2018; Li et al., 2019; Duan et al., 2021). Since the bulk chemical composition of the TSMB did not show evidence of alteration or significant water-rock interactions, it was concluded that metamorphism in the Wuyang rocks approximates a closed system (e.g., Yao et al., 2015; Li et al., 2019; Lan et al., 2019). In this regard, the trace elements and REE + Y characteristics of the TSMB are reliable paleoenvironmental archives of marine chemistry contemporaneous to deposition.

The principal mineral constituent of modern authigenic apatite in marine sediments is carbonate (hydroxy) fluorapatite, $Ca_{10}(PO_4)_{6-x}(CO_3)_x(F,OH)_{2+x}$ (Ruttenberg and Berner, 1993; Mojzsis et al., 1996; März et al., 2018). The REE profile of authigenic sedimentary apatite serves as an indicator of the aqueous environment at the time and location of its deposition, reflecting contemporaneous water chemistry (Piper and Bau, 2013). Generally, during the initial stages of diagenesis, apatite incorporates REEs primarily through surface adsorption, followed by isomorphous substitution of Ca^{2+} within its crystal structure during late-stage diagenetic recrystallization processes (Reynard et al., 1999). In contrast, within the 3.7 Ga Isua BIF in Greenland, secondary hydroxyapatites were implicated in contributing to the anomalously high Nd isotopic signatures observed in the magnetite-dominated layers of the BIF, with ε_{Nd}(t) values of +14.8 and + 14.4 (Frei et al., 1999). This phase, predominantly forming as crystal overgrowths in magnetite-rich bands, significantly impacts the Nd isotopes and Sm/Nd ratios, suggesting an affinity towards REE fractionated, continental sources (Frei et al., 1999). Further, two distinct populations of apatite in the Isua BIF have been identified: sedimentary (diagenetic) and secondary (metasomatic), with the latter exhibiting a distribution pattern enriched in middle REE (Lepland et al., 2002).

The apatite grains within the TSMB display an LREE-enriched pattern, accompanied by Eu and Y anomalies characteristic of marine chemical sediments (Fig. 5). Furthermore, the ε_{Nd}(t) values of apatite in TSMB are relatively low (−6.3 to +1.38), while the ε_{Nd}(t) values of bulk TSMB are relatively low as well (−4.0 to 0, Hu et al., unpublished), indicating that these apatite grains are different from the metasomatic samples in Isua BIF. In sum, these apatite grains have maintained their chemical composition throughout diagenesis and metamorphic processes. Such stability, along with the presence of Eu and Y anomalies, underscores the potential of these apatite grains to record specific marine conditions, including environmental information related to the

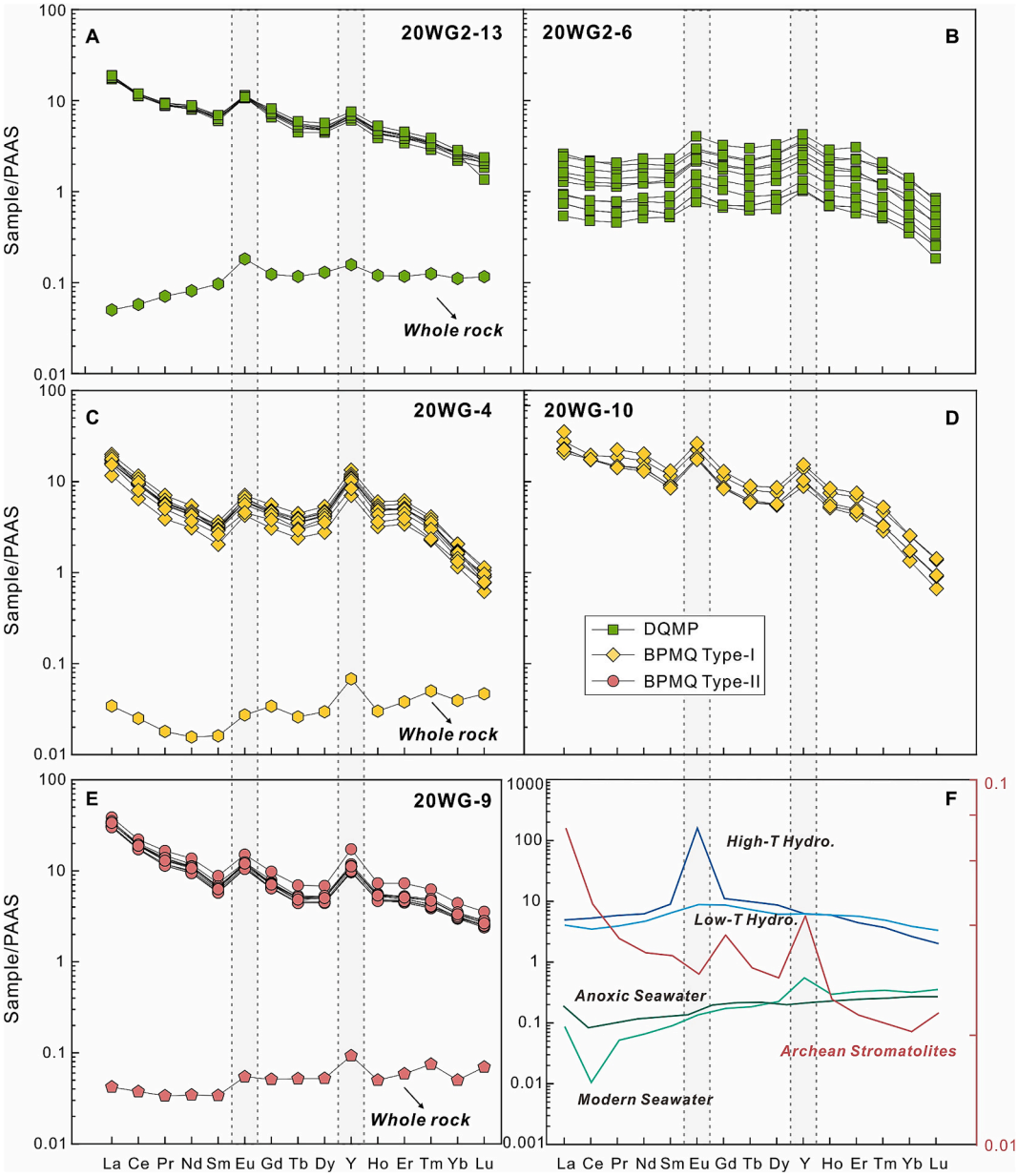

Fig. 5. (A-E) Post-Archean Australian Shale (PAAS; McLennan, 1989) -normalized REE + Y patterns of apatite in comparison with the bulk-BIFs. (F) Values ($\times 10^6$) of different sources of BIFs. High-T and low-T hydrothermal fluid; the average value of 0, 9, 30 m modern seawater in shallow Pacific Ocean; and the average value of 165 and 215 m anoxic seawater in Saanich Inlet (Alibo and Nozaki, 1999; Bau and Dulski, 1999; Bolhar et al., 2004; Bolhar and Van Kranendonk, 2007); The late Archean Stromatolites comes from the average value of Kamber et al., 2004. The corresponding whole rock data comes from Hu, 2024.

redox state of ancient oceans and sources of dissolved REE + Y to seawater.

Regarding the influence of high-grade metamorphism to BIFs, previous studies (e.g., Dauphas et al., 2004; Frost et al., 2007) have shown that while Fe isotopes can be modified by low-temperature metamorphism, the overall compositions often remain relatively preserved when high-temperature metamorphism occurs in a closed system. Furthermore, Fe isotopic homogeneity can be maintained even under granulite-facies conditions in BIFs, as long as fluid-rock interactions are minimal (Planavsky et al., 2012; Czaja et al., 2013). In the Wuyang area, Lan et al. (2019) suggested that the limited fluid-rock interactions did not cause Fe isotopic fractionation in the Wuyang BIFs.

6.2. DIR Recorded by Apatite and Magnetite

The solubility of redox-sensitive elements, such as U and Mn, varies with the redox potential, with Mn precipitating as Mn(III,IV)-oxides (MnO_x) in oxygenated waters overlying a chemocline, while U exists as soluble U(VI)-carbonate-complexes. Under anoxic conditions, U and Mo complex with dissolved organic matter, and U undergoes reduction to U(IV), which either strongly adsorbs onto particles or forms $UO_{2(s)}$ (Anderson, 1982; Albéric et al., 2000; Elbaz-Poulichet et al., 2005). In the modern ocean, U is stable and soluble, primarily removed from seawater by diffusing into sediments and precipitating as insoluble U (IV) following the reduction of U(VI) (Klinkhammer and Palmer, 1991; Mangini et al., 2001). Manganese, in contrast, is soluble as Mn^{2+} in its reduced state, but precipitates as oxides in its oxidized states, Mn^{3+} and Mn^{4+}, in oxygen-rich environments (Calvert and Pedersen, 1996). The reduction of MnO_2 under suboxic conditions releases Mn^{2+} into the overlying waters, leading to an elevated Mn concentration and Mn/U ratio (Elbaz-Poulichet et al., 2005; Chen et al., 2017). Furthermore, the reduction of U(VI) may be facilitated by Fe(III)-reducing bacteria that

Table 1
Apatite Sm—Nd and magnetite Fe isotopes data of Wuyang BIF samples.

Sample	Age(Ga)	$^{147}Sm/^{144}Nd$	2Se	$^{143}Nd/^{144}Nd$	2Se	t_{DM}(Ga)	$\varepsilon_{Nd}(t)$	INd	$\delta^{56}Fe$(‰)	2Se
Banded pyroxene-magnetite quartzite-Type-I										
20WG-10-03	2.45	0.072554	0.000258	0.510691	0.000154	2.640563	0.339744	0.509544		
20WG-10-05	2.45	0.070558	0.000245	0.510663	0.000142	2.63383	0.402921	0.509547		
20WG-10-06	2.45	0.070631	0.000196	0.510526	0.000124	2.778618	−2.30115	0.509409	−0.84	0.02
20WG-10-08	2.45	0.070602	0.000283	0.510433	0.000198	2.875823	−4.12132	0.509316		
20WG-10-09	2.45	0.069587	0.000229	0.51051	0.000145	2.775276	−2.28979	0.50941		
20WG-4-01									−0.62	0.01
Banded pyroxene-magnetite quartzite-Type-II										
20WG-9-01	2.45	0.064012	0.000273	0.510488	0.000175	2.695335	−0.99926	0.509475		
20WG-9-01B	2.45	0.064012	0.000273	0.510488	0.000175	2.695335	−0.99926	0.509475		
20WG-9-02	2.45	0.065919	0.000369	0.510446	0.000201	2.772602	−2.41786	0.509403		
20WG-9-02B	2.45	0.065919	0.000369	0.510446	0.000201	2.772602	−2.41786	0.509403		
20WG-9-03	2.45	0.063309	0.000317	0.510341	0.000182	2.829796	−3.66923	0.509339		
20WG-9-05	2.45	0.062888	0.000322	0.510367	0.00018	2.79563	−3.0192	0.509372		
20WG-9-06	2.45	0.063965	0.000275	0.510352	0.000177	2.830638	−3.6489	0.50934	−2.09	0.02
20WG-9-07	2.45	0.065808	0.000358	0.510307	0.000204	2.911675	−5.11271	0.509266		
20WG-9-07B	2.45	0.065808	0.000358	0.510307	0.000204	2.911675	−5.11271	0.509266		
20WG-9-08	2.45	0.063967	0.000286	0.510247	0.000165	2.936301	−5.71818	0.509235		
20WG-9-08B	2.45	0.063967	0.000286	0.510247	0.000165	2.936301	−5.71818	0.509235		
20WG-9-09	2.45	0.064869	0.000352	0.510319	0.0002	2.881027	−4.57884	0.509293		
20WG-9-10	2.45	0.065154	0.00027	0.510238	0.000161	2.968497	−6.26087	0.509207		
Disseminated quartz magnetite pyroxenite										
20WG-2-13-01	2.45	0.083573	0.000328	0.5107	0.000211	2.8523	−2.91498	0.509378		
20WG-2-13-02	2.45	0.082189	0.000393	0.510686	0.00023	2.8389	−2.76627	0.509385		
20WG-2-13-03	2.45	0.081926	0.000409	0.51075	0.000223	2.760052	−1.42311	0.509454		
20WG-2-13-04	2.45	0.082677	0.000423	0.51076	0.000241	2.76403	−1.45595	0.509452		
20WG-2-13-05	2.45	0.08339	0.000435	0.510797	0.000221	2.735956	−0.94396	0.509478	−0.96	0.01
20WG-2-13-06	2.45	0.082645	0.000437	0.510834	0.000215	2.678684	0.003995	0.509526		
20WG-2-13-07	2.45	0.083508	0.000411	0.510711	0.000209	2.838489	−2.68368	0.509389		
20WG-2-13-08	2.45	0.082419	0.000398	0.5109	0.000229	2.597983	1.379293	0.509597		
20WG-2-13-09	2.45	0.08424	0.000424	0.510727	0.000201	2.835537	−2.59181	0.509394		
20WG-2-13-10	2.45	0.082281	0.000404	0.510772	0.000241	2.742141	−1.09879	0.50947		
20WG-2-6-1-01									−1.36	0.04

Note: $\varepsilon_{Nd}(t) = 10{,}000 \times \{[(^{143}Nd/^{144}Nd\text{-}^{147}Sm/^{144}Nd \times (e^{\lambda t}\text{-}1)]/[(^{143}Nd/^{144}Nd)_{CHUR(0)}\text{-}(^{147}Sm/^{144}Nd)_{CHUR} \times (e^{\lambda t}\text{-}1)]\text{-}1)\}$; $T_{DM} = \ln(1 + (^{143}Nd/^{144}Nd - 0.51315)/(^{147}Sm/^{144}Nd - 0.2137))/(\lambda * 1000000)$.

use ferric iron as an electron acceptor, converting it to Fe^{2+} and thereby impacting its environmental cycling (Lovley et al., 1991). In the TSMB samples, we observed significant differences between Mn and U concentrations (Fig. 6). Specifically, the BQMP-II apatite grains are characterized by higher Mn (637–910 ppm) and lower U (0.66–1.42 ppm) contents, leading to higher Mn/U ratios (467–1210).

Generally, hydrothermal fluids have been inferred as the primary sources of REE + Y and Fe^{2+} during BIF deposition, indicated by their positive $\varepsilon_{Nd}(t)$ values and Eu anomalies (e.g., Bau and Dulski, 1996; Frei and Polat, 2007). However, recent studies on BIFs have shown that there are serval other possibilities for REE + Y and Fe^{2+} sources: (1) continental Fe^{2+} generated via weathering (Li et al., 2015b) or through a benthic Fe shuttle driven by DIR (e.g., Wang, 2024); (2) sea-floor-vented hydrothermal fluids interacting with locally enriched mantle sources (Døssing et al., 2009); (3) hydrothermal fluids interacting with underlying-terrigenous clastic sediments or enriched continental crust (Haugaard et al., 2013; Wang et al., 2014); or (4) some combination of the above mechanisms. The PAAS-normalized REE + Y patterns observed in the TSMB apatite display distinct seawater characteristics influenced by high-temperature hydrothermal fluids, likely representing mixtures of ambient seawater and high-temperature hydrothermal fluids (Fig. 5). Apatite from the DQMP samples exhibit higher $\varepsilon_{Nd}(t)$ values ranging from −2.9 to +1.4, contrasting with BPMQ-I and BPMQ-II apatites which display lower $\varepsilon_{Nd}(t)$ values (−4.1 to +0.4 and − 6.3 to −1.0, respectively). This suggests that the DQMP samples incorporated a greater hydrothermal component during sedimentation compared to the

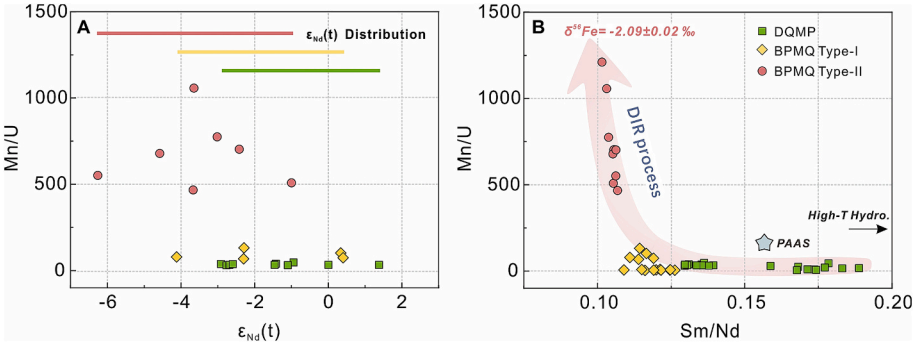

Fig. 6. Plots of trace elements and Nd isotopes in the TSMB apatites. (A) $\varepsilon_{Nd}(t)$ vs. Mn/U; (B) Sm/Nd vs. Mn/U. High-T hydrothermal fluid and PAAS values come from; McLennan, 1989 and Alibo and Nozaki, 1999.

two types of BPMQ samples.

The source of enriched Nd isotopic in BIFs generally is riverine, whose negative $\varepsilon_{Nd}(t)$ values contributed by surface sediments or felsic continental crust (Haugaard et al., 2016) or the DIR-related terrigenous porewater (Severmann et al., 2006). Therefore, the higher $\varepsilon_{Nd}(t)$ values of DQMP samples represent a hydrothermal fluid precipitated end-member, while the lower $\varepsilon_{Nd}(t)$ values of BPMQ samples likely signify terrigenous input to the ambient seawater during deposition. Similar conclusions were reached by Li et al. (2014, 2019) based on the mineralogical and microfabric characteristics of magnetite observed in the TSMB, indicating that quartz-dominant BIFs formed through chemical precipitation during prolonged intervals between volcanic eruptions, while the pyroxene-dominant BIFs resulted from chemical deposition processes influenced directly by volcanic activity.

Given the relatively consistent $\delta^{56}Fe$ value of the upper continental crust (0.12 ± 0.13 ‰) and the negligible Fe isotope variations caused by chemical weathering in this crust (Liu et al., 2022), it is inferred that riverine inputs, resulting from direct weathering of continental materials, would likely possess $\delta^{56}Fe$ values close to zero for dissolved Fe^{2+} (Johnson et al., 2020), akin to those found in hydrothermal fluids (0.15 to 1.2 ‰, Severmann et al., 2004). Hence, a process that actively introduces Fe^{2+} with low-$\delta^{56}Fe$ values into the Archean oceans from continental sources is required, which has been proposed to be the DIR process (e.g., Severmann et al., 2008; Wang et al., 2024). During DIR, Fe (III)-reducing bacteria utilize Fe^{3+} as the electron acceptor for their respiratory activity, reducing Fe^{3+} to Fe^{2+} (Lovley and Phillips, 1988; Balci et al., 2006). Due to the subtle differences in the affinity of the bio-reduction process towards distinct iron isotopes, this can lead to iron isotope ratios in microbial-influenced sediments (such as BIFs) that diverge from those of the surrounding seawater (Taylor and Konhauser, 2011). Specifically, DIR processes often exhibit a preference for the lighter Fe isotope over the heavier one (Johnson et al., 2008) and can result in Fe isotope fractionation up to approximately −3 ‰, enriching dissolved Fe^{2+} in lighter isotopes while leaving behind oxides with higher $\delta^{56}Fe$ values (Severmann et al., 2006; Johnson et al., 2020). The presence of DIR process can be further demonstrated by the significantly negative $\delta^{56}Fe$ values of TSMB samples (−2.1 to −0.62 ‰), which shows a negative correlation with Mn/U ratios (Fig. 7). Hence, the reduced components contributing to the formation of BPMQ-II, evidenced by high Mn/U ratios, negative $\varepsilon_{Nd}(t)$ values and low $\delta^{56}Fe$ values, are likely derived from microbial reduction of Fe(III) and subsequent transportation and deposition via an active submarine iron shuttle. This process highlights the microbial influence on the geochemical signature and sedimentation of BIFs.

Indeed, the occurrence of apatite within some BIFs and its mineralogical characteristics, along with phosphorus's significance as an indicator of early life, and as a crucial macronutrient in primordial oceans, has been recognized (e.g., Sano et al., 1999; Dodd et al., 2019). EDS analyses of apatite and magnetite aggregates in the Dales Gorge BIF in Western Australia by Li et al. (2011), indicate that the source of calcium could be cellular polyphosphate (Brown and Kornberg, 2004), given the lower calcium content in magnetite and surrounding materials compared to the apatite aggregates. Moreover, the detection of strontium hints at a biological origin, due to its preferential incorporation into apatite during biological respiration processes (Li et al., 2011). Finally, P in BIFs may have resulted from its adsorption onto ferric oxyhydroxide particles during the oxidation of Fe^{2+} (Bjerrum and Canfield, 2002; Anand et al., 2014; Jones et al., 2015), although the impacts of highly dissolved silica in the Archean ocean may have led to attenuated P adsorption to Fe(III) oxyhydroxides (see Konhauser et al., 2007 and Jones et al., 2015 for discussion). High concentrations of Sr (15,453 to 20,466 ppm) and OH (33 % to 58 % in molar) in BPMQ-II apatite grains further substantiate its association with biological processes, highlighting the potential for signals of DIR to be recorded in the BIF geological record. These findings underscore the integral role of biological activity in the formation of certain BIFs, indicating a close linkage between microbial activity and mineral deposition.

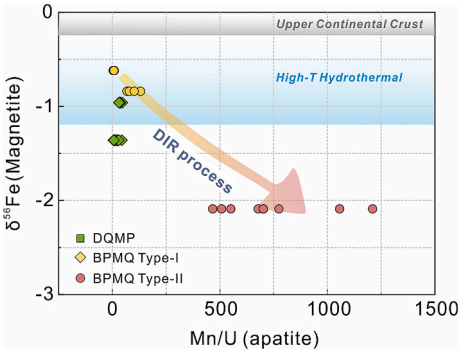

Fig. 7. Plots of magnetite $\delta^{56}Fe$ vs. apatite Mn/U of TSMB samples. High-T hydrothermal fluid and upper continental crust values come from Severmann et al. (2004) and Liu et al. (2022).

7. Conclusions

The distinct negative iron isotopic signatures in magnetite from BIFs of the Tieshanmiao Formation (−2.1 to −0.62 ‰), coupled with the diverse elemental compositions of apatite, offer evidence for the involvement of DIR and emphasize the role of microbial activity during the genesis of BIFs. Moreover, the presence of high Mn/U ratios, alongside elevated Sr and OH contents in apatite, further supports a strong biological influence on the mineralization pathways within these ancient sedimentary deposits. The range and distribution of $\varepsilon_{Nd}(t)$ and $\delta^{56}Fe$ values in the Tieshanmiao Formation BIF samples highlight the significance of continental iron input, supplied through the recycling of iron by DIR and Fe shuttling. This attests to an active consortium of microbes in the late Archean ocean, indicating that the water column and sediments provided the requisite environmental conditions for both Fe^{2+}-oxidizing and Fe^{3+}-reducing microbes to flourish during deposition. Collectively, these findings not only provide significant insights into the biogeochemical cycles of early oceans but also highlight the integral role of microbial communities in shaping Earth's primordial marine environments.

CRediT authorship contribution statement

Tianyang Hu: Writing – original draft. **Leslie J. Robbins:** Writing – review & editing. **Kurt O. Konhauser:** Writing – review & editing. **Lei Liu:** Supervision. **Brendan A. Bishop:** Writing – review & editing. **Guoxiang Chi:** Writing – review & editing. **Lijuan Xu:** Funding acquisition.

Declaration of competing interest

The authors declare that they have no known competing financial interests or personal relationships that could have appeared to influence the work reported in this paper.

Acknowledgements

The authors express their gratitude to the anonymous reviewers, Dr. Marco Fiorentini, and Dr. Eva Stüeken, for their insightful comments that significantly enhanced the quality of this article. This research was supported by the National Natural Science Foundation of China (No. 41972198), the National Natural Science Foundation of Hunan (No. 2022JJ30702), the Post-graduate Research Innovation Project of Hunan (CX20220167) and China Scholarship Council (CSC202206370119). LJR acknowledges support from a Natural Sciences and Engineering Research Council of Canada Discovery Grant (RGPIN-2021-02523). The

authors acknowledge Yuanyou Zhang, and Qifu Wen for their assistance during fieldwork and drill core data collection.

Appendix A. Supplementary data

Supplementary data to this article can be found online at https://doi.org/10.1016/j.chemgeo.2025.122676.

Data availability

Data will be made available on request.

References

Albéric, P., et al., 2000. Interactions between trace elements and dissolved organic matter in the stagnant anoxic deep layer of a meromictic lake. Limnol. Oceanogr. 45 (5), 1088–1096.

Alibo, D.S., Nozaki, Y., 1999. Rare earth elements in seawater: particle association, shale-normalization, and Ce oxidation. Geochim. Cosmochim. Acta 63 (3), 363–372.

Amor, M., et al., 2018. Iron uptake and magnetite biomineralization in the magnetotactic bacterium Magnetospirillum magneticum strain AMB-1: an iron isotope study. Geochim. Cosmochim. Acta 232, 225–243.

Anand, V., et al., 2014. Evaluation of zinc and magnesium doped 45S5 mesoporous bioactive glass system for the growth of hydroxyl apatite layer. J. Non Cryst. Solids 406, 88–94.

Anderson, R.F., 1982. Concentration, vertical flux, and remineralization of particulate uranium in seawater. Geochim. Cosmochim. Acta 46 (7), 1293–1299.

Angerer, T., et al., 2012. Geochemical Evolution of the Banded Iron Formation-Hosted High-Grade Iron Ore System in the Koolyanobbing Greenstone Belt, Western Australia*. Econ. Geol. 107 (4), 599–644.

Balci, N., et al., 2006. Iron isotope fractionation during microbially stimulated Fe(II) oxidation and Fe(III) precipitation. Geochim. Cosmochim. Acta 70 (3), 622–639.

Bau, M., 1991. Rare-earth element mobility during hydrothermal and metamorphic fluid-rock interaction and the significance of the oxidation state of europium. Chem. Geol. 93 (3), 219–230.

Bau, M., Dulski, P., 1996. Distribution of yttrium and rare-earth elements in the Penge and Kuruman iron-formations, Transvaal Supergroup, South Africa. Precambrian Research 79 (1), 37–55.

Bau, M., Dulski, P., 1999. Comparing yttrium and rare earths in hydrothermal fluids from the Mid-Atlantic Ridge: implications for Y and REE behaviour during near-vent mixing and for the Y/Ho ratio of Proterozoic seawater. Chem. Geol. 155 (1), 77–90.

Bilal, B.A., 1991. Thermodynamic Study of Eu3+ /Eu2+ Redox Reaction in Aqueous Solutions at Elevated Temperatures and pressures by Means of Cyclic Voltammetry. Zeitschrift für Naturforschung A 46 (12), 1108–1116.

Bjerrum, C.J., Canfield, D.E., 2002. Ocean productivity before about 1.9 Gyr ago limited by phosphorus adsorption onto iron oxides. Nature 417 (6885), 159–162.

Bolhar, R., Van Kranendonk, M.J., 2007. A non-marine depositional setting for the northern Fortescue Group, Pilbara Craton, inferred from trace element geochemistry of stromatolitic carbonates. Precambrian Res. 155 (3), 229–250.

Bolhar, R., et al., 2004. Characterisation of early Archaean chemical sediments by trace element signatures. Earth Planet. Sci. Lett. 222 (1), 43–60.

Bonnand, P., et al., 2020. Post-depositional REE mobility in a Paleoarchean banded iron formation revealed by La-Ce geochronology: a cautionary tale for signals of ancient oxygenation. Earth Planet. Sci. Lett. 547, 116452.

Brown, M.R.W., Kornberg, A., 2004. Inorganic polyphosphate in the origin and survival of species. Proc. Natl. Acad. Sci. 101 (46), 16085–16087.

Calvert, S.E., Pedersen, T.F., 1996. Sedimentary geochemistry of manganese; implications for the environment of formation of manganiferous black shales. Econ. Geol. 91 (1), 36–47.

Chen, P., et al., 2017. An evaluation of benthic foraminiferal U/ca and U/Mn proxies for deep ocean carbonate chemistry and redox conditions. Geochem. Geophys. Geosyst. 18 (2), 617–630.

Czaja, A.D., et al., 2013. Biological Fe oxidation controlled deposition of banded iron formation in the ca. 3770Ma Isua Supracrustal Belt (West Greenland). Earth Planet. Sci. Lett. 363, 192–203.

Dauphas, N., et al., 2004. Clues from Fe Isotope Variations on the Origin of early Archean BIFs from Greenland. Science 306 (5704), 2077–2080.

Diwu, C.R., et al., 2014. Early Paleoproterozoic (2.45-2.20 Ga) magmatic activity during the period of global magmatic shutdown: Implications for the crustal evolution of the southern North China Craton. Precambrian Res. 255, 627–640.

Dodd, M.S., et al., 2019. Widespread occurrences of variably crystalline 13C-depleted graphitic carbon in banded iron formations. Earth Planet. Sci. Lett. 512, 163–174.

Døssing, L.N. et al., 2009. Characterization of enriched lithospheric mantle components in ~2.7Ga Banded Iron Formations: an example from the Tati Greenstone Belt, Northeastern Botswana. Precambrian Res., 172(3–4): 334–356.

Duan, H., et al., 2021. Insights into characterization and genesis of the Tieshanmiao banded iron formation deposit, China: Evidence from zircon U–Pb dating and geochemistry. Ore Geol. Rev. 138, 104329.

Elbaz-Poulichet, F., et al., 2005. Sedimentary record of redox-sensitive elements (U, Mn, Mo) in a transitory anoxic basin (the Thau lagoon, France). Mar. Chem. 95 (3), 271–281.

Frei, R., Polat, A., 2007. Source heterogeneity for the major components of ~3.7 Ga Banded Iron Formations (Isua Greenstone Belt, Western Greenland): Tracing the nature of interacting water masses in BIF formation. Earth Planet. Sci. Lett. 253 (1), 266–281.

Frei, R., et al., 1999. Controversial Pb-Pb and Sm-Nd isotope results in the early Archean Isua (West Greenland) oxide iron formation: preservation of primary signatures versus secondary disturbances. Geochim. Cosmochim. Acta 63 (3), 473–488.

Friend, C.R.L., et al., 2008. Seawater-like trace element signatures (REE + Y) of Eoarchaean chemical sedimentary rocks from southern West Greenland, and their corruption during high-grade metamorphism. Contrib. Mineral. Petrol. 155 (2), 229–246.

Frost, C.D., et al., 2007. Preservation of Fe isotope heterogeneities during diagenesis and metamorphism of banded iron formation. Contrib. Mineral. Petrol. 153, 211–235.

Griffin, W., 2008. GLITTER: data reduction software for laser ablation ICP-MS. Laser Ablation ICP-MS in the Earth Sciences: current practices outstanding issues(1): 308-311.

Halama, M., et al., 2016. Evaluation of siderite and magnetite formation in BIFs by pressure–temperature experiments of Fe(III) minerals and microbial biomass. Earth Planet. Sci. Lett. 450, 243–253.

Han, C., 2010. Analysis of the exploration perspective in the depth of Wuyang iron deposit, Henan province. Min. Resour. Geol. (02), 150–154.

Haugaard, R., et al., 2013. Petrology and geochemistry of the ~2.9Ga Itilliarsuk banded iron formation and associated supracrustal rocks, West Greenland: source characteristics and depositional environment. Precambrian Res. 229, 150–176.

Haugaard, R., et al., 2016. The nature of Mesoarchaean seawater and continental weathering in 2.85Ga banded iron formation, Slave craton, NW Canada. Geochimica et Cosmochimica Acta 194, 34–56.

Hu, T., 2024. Study on the Genesis of the Great Oxidation Event. In: Evidence from Early Precambrian Continental Evolution and Banded Iron Formation Mineralization on the Southeastern Margin of the North China Craton. Central South University, Hu`nan.

Hu, T., et al., 2024. Coexistence of Algoma- and Superior-type BIFs in back-arc systems: evidence from Xincai, North China Craton. Ore Geology Reviews 171 (1), 106165.

Johnson, C.M., et al., 2005. Experimental constraints on Fe isotope fractionation during magnetite and Fe carbonate formation coupled to dissimilatory hydrous ferric oxide reduction. Geochim. Cosmochim. Acta 69 (4), 963–993.

Johnson, C.M., et al., 2008. Iron isotopes constrain biologic and abiologic processes in banded iron formation genesis. Geochim. Cosmochim. Acta 72 (1), 151–169.

Johnson, C., et al., 2020. Iron Geochemistry: An Isotopic Perspective. Springer.

Jones, C., et al., 2015. Iron oxides, divalent cations, silica, and the early earth phosphorus crisis. Geology 43 (2), 135–138.

Kamber, B.S., et al., 2004. Geochemistry of late Archaean stromatolites from Zimbabwe: evidence for microbial life in restricted epicontinental seas. Precambrian Res. 132 (4), 379–399.

Klinkhammer, G.P., Palmer, M.R., 1991. Uranium in the oceans: where it goes and why. Geochim. Cosmochim. Acta 55 (7), 1799–1806.

Köhler, I., et al., 2013. Biological carbon precursor to diagenetic siderite with spherical structures in iron formations. Nat. Commun. 4 (1), 1741.

Konhauser, K.O., et al., 2005. The potential significance of microbial Fe(III) reduction during deposition of Precambrian banded iron formations. Geobiology 3.

Konhauser, K.O., et al., 2007. Was there really an Archean Phosphate Crisis? Science 315 (5816), 1234.

Konhauser, K.O., et al., 2017. Iron formations: a global record of Neoarchaean to Palaeoproterozoic environmental history. Earth Sci. Rev. 172, 140–177.

Konhauser, K.O., et al., 2023. Logan Medallist 8. Trace elements in Iron Formation as a Window into Biogeochemical Evolution Accompanying the Oxygenation of Earth's Atmosphere. Geosci. Can. 50 (4), 239–258.

Lan, C.Y., et al., 2013. Mineral and geochemical characteristics of the Tieshanmiao-type BIF-iron deposit in Wuyang region of Henan Province and its implications for ore-forming processes. Acta Petrol. Sin. 29 (07), 2567–2582.

Lan, C., et al., 2017. Depositional age and protoliths of the Paleoproterozoic upper Taihua Group in the Wuyang area in the southern margin of the North China Craton: New insights into stratigraphic subdivision and tectonic setting. Precambrian Res. 297 (297), 77–100.

Lan, C., et al., 2019. In-site mineral geochemistry and whole-rock Fe isotopes of the quartz-magnetite-pyroxene rocks in the Wuyang area, North China Craton: Constraints on the genesis of the pyroxene-rich BIF. Precambrian Res. 333, 105445.

Lepland, A., et al., 2002. Apatite in early Archean Isua supracrustal rocks, southern West Greenland: its origin, association with graphite and potential as a biomarker. Precambrian Res. 118 (3), 221–241.

Lepland, A., et al., 2005. Questioning the evidence for Earth's earliest life—Akilia revisited. Geology 33 (1), 77–79.

Li, Y., et al., 2011. Mineral ecophysiological data provide growing evidence for microbial activity in banded-iron formations. Geology 39 (8), 707–710.

Li, Y., et al., 2013a. Experimental low-grade alteration of biogenic magnetite indicates microbial involvement in generation of banded iron formations. Earth Planet. Sci. Lett. 361, 229–237.

Li, Y., et al., 2013b. Geochemistry of Tieshan Iron Deposit in the Wuyang Area, Henan Province and its Environmental Implications. Acta Geologica Sinica(09), 1377–1398.

Li, H., et al., 2014. Mineralogical and microfabric characteristics of magnetite in the Wuyang Precambrian BIFs, southern North China Craton: Implications for genesis and depositional processes of the associated BIFs. J. Asian Earth Sci. 94 (0), 267–281.

Li, H., et al., 2015a. Desilicification and iron activation–reprecipitation in the high-grade magnetite ores in BIFs of the Anshan-Benxi area, China: evidence from geology,

geochemistry and stable isotopic characteristics. J. Asian Earth Sci. 113 (Part 3), 998–1016.
Li, W., et al., 2015b. Biologically recycled continental iron is a major component in banded iron formations. Proc. Natl. Acad. Sci. 112 (27), 8193–8198.
Li, H., et al., 2019. The mineralogy, mineral chemistry, and origin of the Wuyang banded iron formations, North China Craton. Precambrian Res. 328, 111–127.
Li, Y., et al., 2021. A novel approach to investigate the deposition of (bio)chemical sediments: the sedimentation velocity of cyanobacteria–ferrihydrite aggregates. J. Sediment. Res. 91 (4), 390–398.
Li, X., et al., 2022. High-precision Fe isotope analysis on MC-ICPMS using a 57Fe-58Fe double spike technique. Metabolism 20, 22.
Li, Y., et al., 2024. Cyanobacteria-ferrihydrite aggregates, BIF sedimentation and implications for Archaean-Palaeoproterozoic seawater geochemistry. S. Afr. J. Geol. 127 (2), 359–378.
Liu, L., et al., 2018. Age, origin and significance of the Wugang BIF in the Taihua complex, Southern North China Craton. Ore Geol. Rev. 95, 880–898.
Liu, X.M., et al., 2022. Constant iron isotope composition of the upper continental crust over the past 3 Gyr. Geochem. Perspect. Lett. 22, 16–19.
Lovley, D.R., Phillips, E.J.P., 1988. Novel mode of microbial energy metabolism: organic carbon oxidation coupled to dissimilatory reduction of iron or manganese. Appl. Environ. Microbiol. 54 (6), 1472–1480.
Lovley, D.R., et al., 1991. Microbial reduction of uranium. Nature 350 (6317), 413–416.
MacRae, N.D., et al., 1992. Development of a positive Eu anomaly during diagenesis. Earth Planet. Sci. Lett. 109 (3), 585–591.
Mangini, A., et al., 2001. What do we learn from peaks of uranium and of manganese in deep sea sediments? Mar. Geol. 177 (1), 63–78.
Martins, P.L.G., et al., 2022. Chemostratigraphy of the Carajás banded iron formation, Brazil: a record of Neoarchean Ocean chemistry. Gondw. Res. 105, 217–242.
März, C., et al., 2018. Phosphorus dynamics around the sulphate-methane transition in continental margin sediments: Authigenic apatite and Fe(II) phosphates. Mar. Geol. 404, 84–96.
McLennan, S.M., 1989. Chapter 7. Rare earth elements in sedimentary rocks: influence of provenance and sedimentary processes. In: Bruce, R.L., McKay, G.A. (Eds.), Geochemistry and Mineralogy of Rare Earth Elements. De Gruyter, Berlin, Boston, pp. 169–200.
Mojzsis, S.J., et al., 1996. Evidence for life on Earth before 3,800 million years ago. Nature 384 (6604), 55–59.
Möller, P., 1983. Lanthanoids as a Geochemical Probe and Problems in Lanthanoid Geochemistry distribution and Behaviour of Lanthanoids in Non-Magmatic-Phases. In: Sinha, S.P. (Ed.), Systematics and the Properties of the Lanthanides. Springer, Netherlands, Dordrecht, pp. 561–616.
Pecoits, E., et al., 2009. Petrography and geochemistry of the Dales Gorge banded iron formation: Paragenetic sequence, source and implications for palaeo-ocean chemistry. Precambrian Res. 172 (1), 163–187.
Piper, D.Z., Bau, M., 2013. Normalized rare earth elements in water, sediments, and wine: identifying sources and environmental redox conditions. Am. J. Anal. Chem. 2013.
Planavsky, N., et al., 2010. Rare Earth Element and yttrium compositions of Archean and Paleoproterozoic Fe formations revisited: New perspectives on the significance and mechanisms of deposition. Geochim. Cosmochim. Acta 74 (22), 6387–6405.
Planavsky, N., et al., 2012. Iron isotope composition of some Archean and Proterozoic iron formations. Geochim. Cosmochim. Acta 80, 158–169.
Posth, N.R., et al., 2014. Biogenic Fe(III) minerals: from formation to diagenesis and preservation in the rock record. Earth Sci. Rev. 135, 103–121.
Rasmussen, B., et al., 2017. Greenalite precipitation linked to the deposition of banded iron formations downslope from a late Archean carbonate platform. Precambrian Res. 290, 49–62.
Rasmussen, B., et al., 2021a. Greenalite and its role in the genesis of early Precambrian iron formations – a review. Earth Sci. Rev. 217, 103613.
Rasmussen, B., et al., 2021b. Apatite nanoparticles in 3.46–2.46 Ga iron formations: evidence for phosphorus-rich hydrothermal plumes on early Earth. Geology 49 (6), 647–651.
Reynard, B., et al., 1999. Crystal-chemical controls on rare-earth element concentrations in fossil biogenic apatites and implications for paleoenvironmental reconstructions. Chem. Geol. 155 (3), 233–241.
Roy, S., Venkatesh, A.S., 2009. Mineralogy and geochemistry of banded iron formation and iron ores from eastern India with implications on their genesis. J. Earth Syst. Sci. 118 (6), 619–641.
Rudnick, R.L., et al., 1985. Large ion lithophile elements in rocks from high-pressure granulite facies terrains. Geochim. Cosmochim. Acta 49 (7), 1645–1655.
Ruttenberg, K.C., Berner, R.A., 1993. Authigenic apatite formation and burial in sediments from non-upwelling, continental margin environments. Geochim. Cosmochim. Acta 57 (5), 991–1007.
Sano, Y., et al., 1999. Origin of life from apatite dating? Nature 400 (6740), 127–128.
Severmann, S., et al., 2004. The effect of plume processes on the Fe isotope composition of hydrothermally derived Fe in the deep ocean as inferred from the Rainbow vent site, Mid-Atlantic Ridge, 36 degrees 14' N. Earth Planet. Sci. Lett. 225 (1–2), 63–76.
Severmann, S., et al., 2006. The effect of early diagenesis on the Fe isotope compositions of porewaters and authigenic minerals in continental margin sediments. Geochim. Cosmochim. Acta 70 (8), 2006–2022.
Severmann, S., et al., 2008. Modern iron isotope perspective on the benthic iron shuttle and the redox evolution of ancient oceans. Geology 36 (6), 487–490.
Steinhoefel, G., et al., 2010. Deciphering formation processes of banded iron formations from the Transvaal and the Hamersley successions by combined Si and Fe isotope analysis using UV femtosecond laser ablation. Geochim. Cosmochim. Acta 74 (9), 2677–2696.
Taylor, K.G., Konhauser, K.O., 2011. Iron in Earth Surface Systems: a Major Player in Chemical and Biological Processes. Elements 7 (2), 83–88.
Thompson, K.J., et al., 2019. Photoferrotrophy, deposition of banded iron formations, and methane production in Archean oceans. Sci. Adv. 5 (11), 2869.
Trendall, A.F., Morris, R.C., 1983. Iron-Formation: Facts and Problems. Elsevier.
Vargas, M., et al., 1998. Microbiological evidence for Fe(III) reduction on early Earth. Nature 395 (6697), 65–67.
Wan, Y., et al., 2012. Formation Ages of early Precambrian BIFs in the North China Craton: SHRIMP Zircon U-Pb Dating. Acta Geol. Sin. 86 (09), 1447–1478.
Wang, C., et al., 2014. Source characteristics of the ~2.5Ga Wangjiazhuang Banded Iron Formation from the Wutai greenstone belt in the North China Craton: evidence from neodymium isotopes. J. Asian Earth Sci. 93, 288–300.
Wang, C., et al., 2024. Late Archean Shelf-to-Basin Iron shuttle Contributes to the Formation of the World-Class Dataigou Banded Iron Formation. Econ. Geol. 119 (3), 725–736.
Yang, Y.-H., et al., 2014. Sr and Nd isotopic compositions of apatite reference materials used in U–Th–Pb geochronology. Chem. Geol. 385, 35–55.
Yao, T., et al., 2015. Origin of the disseminated magnetite pyroxenite in the Tieshanmiao-type iron deposits in the Wuyang region of Henan Province, China. J. Asian Earth Sci. 113 (0), 1235–1252.
Zhai, M., Windley, B.F., 1990. The Archaean and early Proterozoic banded iron formations of North China: their characteristics, geotectonic relations, chemistry and implications for crustal growth. Precambrian Res. 48 (3), 267–286.
Zhang, L., et al., 2012. Study of the Precambrian BIF-iron deposits in the North China Craton: Progresses and questions. Acta Petrol. Sin. 28 (11), 3431–3445.
Zhang, Z., et al., 2014. Spatio-temporal distribution and tectonic settings of the major iron deposits in China: an overview. Ore Geol. Rev. 57, 247–263.
Zhao, G., et al., 2005. Late Archean to Paleoproterozoic evolution of the North China Craton: key issues revisited. Precambrian Res. 136 (2), 177–202.